Local electronic and magnetic properties of the doped topological insulators Bi_2Se_3:Ca and Bi_2Te_3:Mn investigated using ion-implanted ^{8}Li β-NMR

Ryan M. L. McFadden,[1,2,*] Aris Chatzichristos,[2,3] David L. Cortie,[1,2,3,†] Derek Fujimoto,[2,3] Yew San Hor,[4] Huiwen Ji,[5,‡] Victoria L. Karner,[1,2] Robert F. Kiefl,[2,3,6] C. D. Philip Levy,[6] Ruohong Li,[6] Iain McKenzie,[6,7] Gerald D. Morris,[6] Matthew R. Pearson,[6] Monika Stachura,[6] Robert J. Cava,[5] and W. Andrew MacFarlane[1,2,6,§]

[1]*Department of Chemistry, University of British Columbia, Vancouver, BC V6T 1Z1, Canada*
[2]*Stewart Blusson Quantum Matter Institute, University of British Columbia, Vancouver, BC V6T 1Z4, Canada*
[3]*Department of Physics and Astronomy, University of British Columbia, Vancouver, BC V6T 1Z1, Canada*
[4]*Department of Physics, Missouri University of Science and Technology, Rolla, Missouri 65409, USA*
[5]*Department of Chemistry, Princeton University, Princeton, New Jersey 08544, USA*
[6]*TRIUMF, 4004 Wesbrook Mall, Vancouver, BC V6T 2A3, Canada*
[7]*Department of Chemistry, Simon Fraser University, Burnaby, BC V5A 1S6, Canada*

(Received 22 January 2020; accepted 8 December 2020; published 28 December 2020)

We report β-NMR measurements in Bi_2Se_3:Ca and Bi_2Te_3:Mn single crystals using $^8Li^+$ implanted to depths on the order of 100 nm. Above ~200 K, spin-lattice relaxation reveals diffusion of $^8Li^+$, with activation energies of ~0.4 eV (~0.2 eV) in Bi_2Se_3:Ca (Bi_2Te_3:Mn). At lower temperatures, the NMR properties are those of a heavily doped semiconductor in the metallic limit, with Korringa relaxation and a small, negative, temperature-dependent Knight shift in Bi_2Se_3:Ca. From this, we make a detailed comparison with the isostructural tetradymite Bi_2Te_2Se [McFadden *et al.*, Phys. Rev. B **99**, 125201 (2019)]. In the magnetic Bi_2Te_3:Mn, the effects of the dilute Mn moments predominate, but remarkably the ^{8}Li signal is not wiped out through the magnetic transition at 13 K, with a prominent critical peak in the spin-lattice relaxation that is suppressed in a high applied field. This detailed characterization of the ^{8}Li NMR response is an important step toward using depth-resolved β-NMR to study the low-energy properties of the chiral topological surface state in the Bi_2Ch_3 tetradymite topological insulator.

DOI: 10.1103/PhysRevB.102.235206

I. INTRODUCTION

The bismuth chalcogenides Bi_2Ch_3 (Ch = S, Se, or Te) of the layered tetradymite structure are an interesting class of highly two-dimensional narrow-band-gap semiconductors. Strong spin-orbit coupling inverts the energy ordering of their bands, making them bulk topological insulators (TIs) characterized by a single Dirac cone at the Brillouin zone center and a topologically protected metallic surface state [1,2]. This has augmented long-standing interest in their thermoelectric properties with significant efforts (theoretical and experimental) to understand their electronic properties in detail [3,4]. Consisting of weakly interacting Ch-Bi-Ch-Bi-Ch atomic quintuple layers (QLs) (see, e.g., Fig. 1 in Ref. [5]), they can also accommodate intercalant species such as Li^+ in the van der Waals (vdW) gap between QLs [6–8], similar to the layered transition metal dichalcogenides (TMDs) [9,10]. Although their band gaps are ~150 meV, doping by intrinsic defects, such as Ch vacancies, yields crystals that are far from insulating. To increase the contrast in conductivity between the bulk and the metallic topological surface state (TSS), the crystals are often compensated extrinsically. For example, Ca substitution for Bi suppresses the self-doped n-type conductivity in Bi_2Se_3 [1,11]. Doping can also be used to modulate their magnetic properties, yielding magnetic TIs where the TSS is gapped [12], for example by substitution of Bi with a paramagnetic transition metal [13,14].

The intriguing electronic properties of the tetradymite TIs have predominantly been investigated using surface-sensitive probes in real and reciprocal space [e.g., scanning tunneling spectroscopy (STS) and angle-resolved photoemission spectroscopy (ARPES)], as well as other bulk methods. As a complement to these studies, nuclear magnetic resonance (NMR) offers the ability to probe their electronic ground state and low-energy excitations through the hyperfine coupling of the nuclear spin probe to the surrounding electrons. Such a local probe is especially useful when disorder masks sharp reciprocal space features, as is the case in Bi_2Ch_3. The availability of a useful NMR nucleus, however, is usually determined by elemental composition and natural (or enriched) isotopic abundance, as well as the specific nuclear properties such as the gyromagnetic ratio γ and, for spin $>1/2$, the nuclear electric quadrupole moment Q. While the Bi_2Ch_3

*rmlm@chem.ubc.ca
†Present address: Institute for Superconducting and Electronic Materials, Australian Institute for Innovative Materials, University of Wollongong, North Wollongong NSW 2500, Australia.
‡Present address: Department of Materials Science and Engineering, University of California, Berkeley, Berkeley, CA 94720, USA.
§wam@chem.ubc.ca

 ©2020 American Physical Society

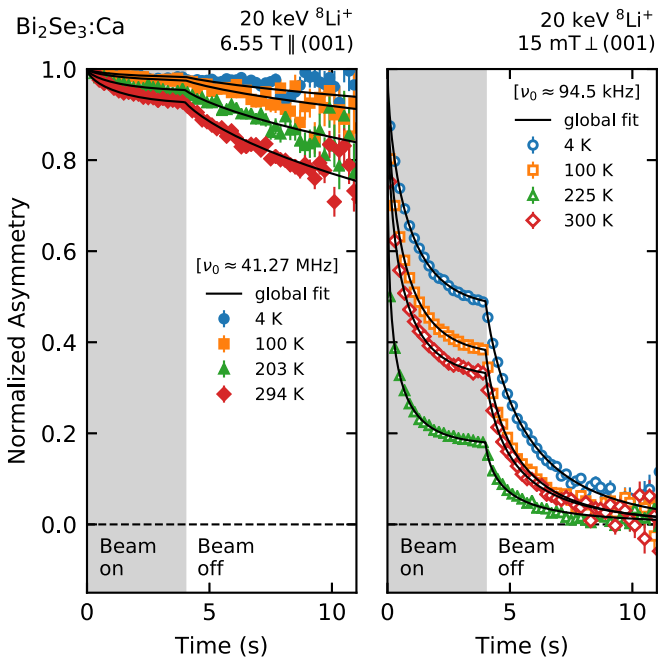

FIG. 1. Typical ^{8}Li SLR spectra in Ca-doped Bi_2Se_3 at high (left) and low (right) magnetic field with $^8Li^+$ implanted at 20 keV. The shaded region indicates the duration of the $^8Li^+$ beam pulse. The relaxation is strongly field-dependent, increasing at lower fields, and it increases nonmonotonically with increasing temperature. The solid black lines show fits to a stretched exponential described in the text. The initial asymmetry A_0 from the fits is used to normalize the data, which are binned by a factor of 20 for clarity.

family naturally contains several NMR nuclei [15–17], they are either low-abundance or have a large Q. As an alternative, here we use an ion-implanted NMR probe at ultratrace concentrations, with detection based on the asymmetric property of radioactive β-decay, known as β-detected nuclear magnetic resonance (β-NMR) [18].

A key feature of ion-implanted β-NMR is the depth resolution afforded by control of the incident beam energy [18,19], which dictates the stopping distribution of the implanted NMR probes. At keV energies, the depth can be varied on the nanometer length-scale, and, at the lowest accessible energies, it may be able to sense the TSS in the tetradymite TIs, which is likely confined to depths <1 nm below the surface. Here one expects Korringa relaxation and Knight shifts from the TSS electrons, modified by the phase space restrictions imposed by their chirality. The magnitude of each will depend on both the TSS carrier density and the strength of the coupling to the implanted nuclei. While the motivation to study the TSS is strong, here we report the "bulk" response of an implanted ^{8}Li probe in two doped Bi_2Ch_3 TIs. This is an essential step toward detecting the TSS [5,20], but it also demonstrates the sensitivity of the implanted ^{8}Li to the carriers in such heavily compensated narrow gap semiconductors.

Using β-NMR, we study two single crystals of doped Bi_2Ch_3—compensated Bi_2Se_3:Ca (BSC) and magnetic Bi_2Te_3:Mn (BTM)—each with a beam of highly polarized $^8Li^+$. In many respects, β-NMR is closely related to muon spin rotation/relaxation/resonance (μSR), but the radioactive lifetime is much longer, making the frequency range of dynamics it is sensitive to more comparable to conventional NMR. In addition to purely electronic phenomena, in solids containing mobile species, NMR is also well known for its sensitivity to low-frequency diffusive fluctuations [21–23], as are often encountered in intercalation compounds. At ion-implantation energies sufficient to probe the bulk of BSC and BTM, we find evidence for ionic mobility of $^8Li^+$ above ~200 K, likely due to two-dimensional (2D) diffusion in the vdW gap. At low temperature, we find Korringa relaxation and a small temperature-dependent negative Knight shift in BSC, allowing a detailed comparison with ^{8}Li in the structurally similar Bi_2Te_2Se (BTS) [5]. In BTM, the effects of the Mn moments predominate, but remarkably the signal can be followed through the magnetic transition. At low temperature, we find a prominent critical peak in the relaxation that is suppressed in a high applied field, and a broad, intense resonance that is strongly shifted. This detailed characterization of the ^{8}Li NMR response is an important step toward using depth-resolved β-NMR to study the low-energy properties of the chiral TSS.

II. EXPERIMENT

Doped TI single crystals BSC and BTM with nominal stoichiometries $Bi_{1.99}Ca_{0.01}Se_3$ and $Bi_{1.9}Mn_{0.1}Te_3$ were grown as described in Refs. [11,13] and magnetically characterized using a Quantum Design magnetic property measurement system (MPMS). In the BTM, a ferromagnetic transition was identified at $T_C \approx 13$ K, consistent with similar Mn concentrations [13,24–26]. In contrast, the susceptibility of the BSC crystal was too weak to measure accurately, but the data show no evidence for a Curie tail at low-T that could originate from dilute paramagnetic defects.

β-NMR experiments were performed at TRIUMF's isotope separator and accelerator (ISAC) facility in Vancouver, Canada. Detailed accounts of the technique can be found in Refs. [5,18]. A low-energy highly polarized beam of $^8Li^+$ was implanted into the samples mounted in one of two dedicated spectrometers [18,19]. Prior to mounting, the crystals were cleaved in air and affixed to sapphire plates using Ag paint (SPI Supplies, West Chester, PA). The approximate crystal dimensions were 7.8 mm × 2.5 mm × 0.5 mm (BSC) and 5.3 mm × 4.8 mm × 0.5 mm (BTM). With the crystals attached, the plates were then clamped to an aluminum holder threaded into an ultrahigh vacuum (UHV) helium coldfinger cryostat. The incident $^8Li^+$ ion beam had a typical flux of $\sim 10^6$ ions/s over a beam spot ~2 mm in diameter. At the implantation energies E used here (between 1 and 25 keV), $^8Li^+$ stopping profiles were simulated for 10^5 ions using the SRIM Monte Carlo code (see Appendix A) [27]. For $E > 1$ keV, a negligible fraction of the $^8Li^+$ stops near enough to the crystal surface to sense the TSS. Most of the data are taken at 20 keV, where the implantation depth is ~100 nm, and the results thus reflect the bulk behavior.

The probe nucleus ^{8}Li has nuclear spin $I = 2$, gyromagnetic ratio $\gamma/2\pi = 6.3016$ MHz T^{-1}, nuclear electric quadrupole moment $Q = +32.6$ mb, and radioactive lifetime $\tau_\beta = 1.21$ s. The nuclear spin is polarized in-flight by collinear optical pumping with circularly polarized

light [28], yielding a polarization of ∼70% [29]. In each measurement, we alternate the sense of circular polarization (left and right) of the pumping light, producing either "positive" or "negative" helicity in the ^{8}Li beam (i.e., its nuclear spin polarization is aligned or counter-aligned with the beam). Data were collected separately for each helicity, which are usually combined, but in some cases they are considered independently to reveal "helicity-resolved" properties. While helicity-resolved spectra are useful to elucidate details of resonance lines (see Appendix B), combined spectra are helpful to remove detection systematics (see, e.g., [18,30]). The ^{8}Li polarization was monitored after implantation through the anisotropic radioactive β-decay, similar to μSR. Specifically, the experimental asymmetry A (proportional to the average longitudinal spin-polarization) was measured by combining the rates in two opposed scintillation counters [18,30]. The proportionality constant depends on the experimental geometry and the details of the β-decay (here, on the order of ∼0.1).

Spin-lattice relaxation (SLR) measurements were performed by monitoring the transient decay of spin-polarization both during and following a pulse of beam lasting several seconds. During the pulse, the polarization approaches a steady-state value, while after the pulse, it relaxes to essentially zero. At the edge of the pulse, there is a discontinuity in the slope, characteristic of β-NMR SLR spectra (see, e.g., Fig. 1). Note that unlike conventional NMR, no radiofrequency (RF) field is required for the SLR measurements. As a result, it is generally more expedient to measure SLR than the resonance; however, there is no spectral resolution of the relaxation, which represents the SLR of all the ^{8}Li. The temperature dependence of the SLR rate was measured at several applied magnetic fields B_0: 6.55 T parallel to the Bi_2Ch_3 trigonal c-axis; and at lower fields ⩽20 mT perpendicular to the c-axis. A typical SLR measurement took ∼20 min.

Resonances were acquired using a direct current (DC) ^{8}Li$^+$ beam and a continuous wave (CW) transverse RF magnetic field B_1. In this measurement mode, the RF frequency is stepped slowly through the ^{8}Li Larmor frequency

$$\omega_0 = 2\pi\nu_0 = \gamma B_0,$$

and the spin of any on-resonance ^{8}Li is rapidly precessed, resulting in a loss in the average time-integrated β-decay asymmetry. The resonance amplitudes are determined by several factors: the baseline asymmetry (i.e., the time integral of the SLR); the RF amplitude B_1; the presence of slow, spectral ^{8}Li dynamics occurring up to the second timescale (see, e.g., Ref. [31]); and, for quadrupole satellite transitions, the relative populations of the magnetic sublevels, which are somewhat different than conventional pulsed NMR [5,18,32]. Resonances were recorded over a temperature range of 4–315 K at both high and low magnetic fields. At high field, the resonance frequency was calibrated against its position in a single crystal of MgO at 300 K, with the superconducting solenoid persistent. A single spectrum typically took ∼30 min to acquire.

III. RESULTS AND ANALYSIS

A. Bi_2Se_3:Ca

Typical ^{8}Li SLR spectra in BSC, at both high and low magnetic field, are shown in Fig. 1. To aid comparison, $A(t)$ has been normalized by its initial value A_0 determined from fits described below. Clearly, the SLR is strongly temperature- and field-dependent. At low field, the SLR is very much faster, due to additional relaxation from fluctuations of the host lattice nuclear spins [33]. The temperature dependence of the relaxation is nonmonotonic, indicating that some of the low-frequency fluctuations at ω_0 are frozen out at low temperature.

The relaxation is nonexponential at *all* temperatures *and* fields, so the data were fit with the phenomenological stretched exponential. This approach was also used for ^{8}Li in BTS [5] and in conventional NMR of related materials [15–17]. Explicitly, for a ^{8}Li$^+$ implanted at time t', the spin polarization at time $t > t'$ follows:

$$R(t,t') = \exp\{-[\lambda(t-t')]^\beta\}, \tag{1}$$

where $\lambda \equiv 1/T_1$ is the SLR rate and $0 < \beta \leqslant 1$ is the stretching exponent. This is the simplest model that fits the data well with the minimal number of free parameters, for the entire Bi_2Ch_3 tetradymite family of TIs.

Using Eq. (1) convoluted with the beam pulse, SLR spectra in BSC, grouped by magnetic field B_0 and implantation energy E, were fit simultaneously with a shared common initial asymmetry $A_0(B_0, E)$. Note that the statistical uncertainties in the data are strongly time-dependent (see, e.g., Fig. 1), which must be accounted for in the analysis. Using custom C++ code incorporating the MINUIT minimization routines [34] implemented within the ROOT data analysis framework [35], we find the global least-squares fit for each dataset. The fit quality is good ($\tilde{\chi}^2_{\text{global}} \approx 1.02$), and a subset of the results are shown in Fig. 1 as solid black lines. The large values of A_0 extracted from the fits (∼10% for $B_0 = 6.55$ T and ∼15% for $B_0 = 15$ mT) are consistent with the full beam polarization, with no missing fraction. The fit parameters are plotted in Fig. 2, showing agreement with the qualitative observations above.

We now consider a model for the temperature and field dependence of $1/T_1$. We interpret the local maxima in $1/T_1$ in Fig. 2 as Bloembergen-Purcell-Pound (BPP) peaks [21], caused by a fluctuating field coupled to the ^{8}Li nuclear spin with a characteristic rate that sweeps through ω_0 at the peak temperature [21,36,37]. Potential sources of the fluctuations are discussed below. The rate peaks are superposed on a smooth background that is approximately linear, reminiscent of Korringa relaxation in metals [32,38]. This is surprising, since BSC is a semiconductor, but it is similar to BTS [5]. We discuss this point further in Sec. IV B.

From this, we adopt the following model for the total SLR rate:

$$1/T_1 = a + bT + \sum_i c_i(J_{1,i} + 4J_{2,i}). \tag{2}$$

In Eq. (2), the first two terms account for the T-linear contribution with a finite intercept a, while the remaining terms describe the ith $1/T_1$ peak in terms of a coupling constant

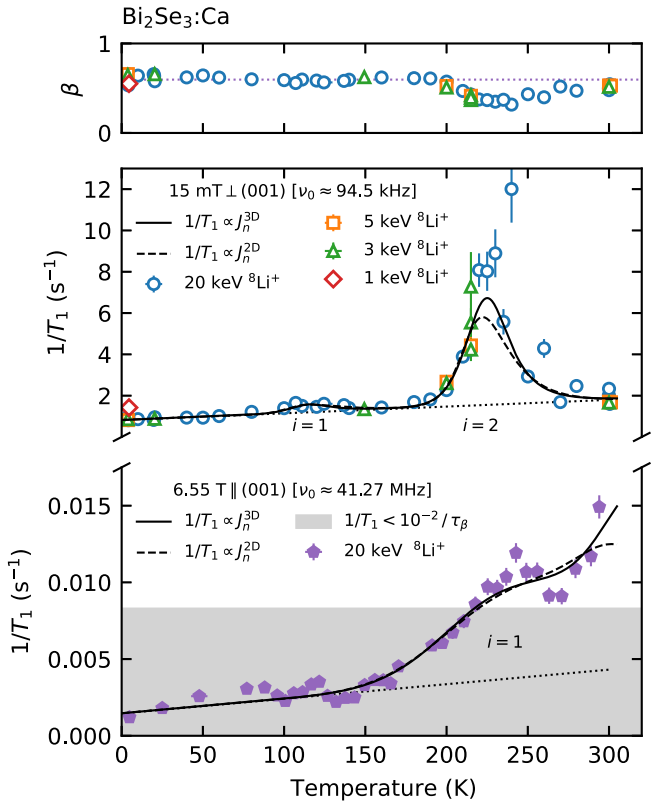

FIG. 2. Temperature and field dependence of the ^{8}Li SLR rate $1/T_1$ and stretching exponent β in Ca-doped Bi_2Se_3. β is nearly independent of temperature and field at ∼0.6 (dotted line), except at low field around the large $1/T_1$ peak seen in the bottom panel. The solid and dashed black lines are global fits to Eq. (2), consisting of a linear T-dependence with a nonzero intercept and two SLR rate peaks, labeled with index i. Independent of the choice of J_n used in the analysis, the model captures all the main features of the data. The T-linear contribution to $1/T_1$ is shown as the dotted black line.

c_i (proportional to the mean-squared transverse fluctuating field) and the n-quantum NMR spectral density functions $J_{n,i}$ [37]. In general, $J_{n,i}$ is frequency-dependent and peaked at a temperature where the fluctuation rate matches $\sim n\omega_0$. While the precise form of $J_{n,i}$ is not known *a priori*, the simplest expression, obtained for isotropic three-dimensional (3D) fluctuations, has a Debye (Lorentzian) form [21,37]

$$J_n^{3D} = \frac{\tau_c}{1 + (n\omega_0\tau_c)^2}, \tag{3}$$

where τ_c is the (exponential) correlation time of the fluctuations. Alternatively, when the fluctuations are 2D in character, as might be anticipated for such a layered crystal, J_n may be described by the empirical expression [36,39]

$$J_n^{2D} = \tau_c \ln(1 + (n\omega_0\tau_c)^{-2}). \tag{4}$$

For both Eqs. (3) and (4), we assume that τ_c is thermally activated, following an Arrhenius dependence:

$$\tau_c^{-1} = \tau_0^{-1} \exp\left(-\frac{E_A}{k_B T}\right), \tag{5}$$

TABLE I. Arrhenius parameters in Eq. (5) obtained from the analysis of the temperature dependence of $1/T_1$ in Ca-doped Bi_2Se_3 shown in Fig. 2. The two processes giving rise to the rate peaks are labeled with index i. Good agreement is found between the E_A's determined using the spectral density functions J_n for 2D and 3D fluctuations [Eqs. (3) and (4)].

	$i = 1$		$i = 2$	
J_n	τ_0^{-1} (10^{10} s^{-1})	E_A (eV)	τ_0^{-1} (10^{14} s^{-1})	E_A (eV)
3D	8.4 ± 2.7	0.113 ± 0.005	7 ± 5	0.395 ± 0.015
2D	9 ± 3	0.106 ± 0.005	110 ± 90	0.430 ± 0.016

where E_A is the activation energy, τ_0 is a prefactor, and k_B is the Boltzmann constant. If the fluctuations are due to $^8Li^+$ hopping, τ_c^{-1} is the site-to-site hop rate.

Using the above expressions, we fit the $1/T_1$ data using a global procedure wherein the kinetic parameters (i.e., $E_{A,i}$ and $\tau_{0,i}^{-1}$) are shared at all the different ω_0. This was necessary to fit the data at 6.55 T where the relaxation is very slow. For comparison, we applied this procedure using both J_n^{3D} and J_n^{2D} and the fit results are shown in Fig. 2 as solid (J_n^{3D}) and dashed (J_n^{2D}) lines, clearly capturing the main features of the data. The analysis distinguishes two processes, $i = 1, 2$ in Eq. (2): one ($i = 1$) that onsets at lower temperature with a shallow Arrhenius slope of ∼0.1 eV that yields the weaker peaks in $1/T_1$ at both fields; and a higher barrier process ($i = 2$) with an E_A of ∼0.4 eV that yields the more prominent peak in the low-field relaxation, while the corresponding high-field peak must lie above the accessible temperature range. The resulting fit parameters are given in Table I. We discuss the results in Sec. IV A.

We now turn to the ^{8}Li resonances, with typical spectra shown in Fig. 3. As anticipated for a noncubic crystal, the spectrum is quadrupole split, confirmed unambiguously by the helicity-resolved spectra (see Fig. 10 in Appendix B). This splitting, on the order of a few kHz [40], is determined by the electric field gradient (EFG) and is a signature of the crystallographic ^{8}Li site. Besides this, an unsplit component is also apparent, very close to (within ∼100 Hz) the center-of-mass of the four satellites. At low temperature, the "central" and split components are nearly equal, but as the temperature is raised, the unsplit line grows to dominate the spectrum, accompanied by a slight narrowing.

The scale of the quadrupole splitting is determined by the product of the principal component of the EFG tensor eq with the nuclear electric quadrupole moment eQ. We quantify this with a conventional definition of the quadrupole frequency (for $I = 2$) [42]:

$$\nu_q = \frac{e^2qQ}{8h}.$$

In high field, a first-order perturbation treatment of the quadrupole interaction is sufficient to obtain accurate satellite positions. However, at low field, where $\nu_q/\nu_0 \approx 6\%$, second-order terms are required [42,43]. Based on the change in satellite splittings by a factor 2 in going from $B_0 \parallel c$ to $B_0 \perp c$, we assume the asymmetry parameter of the EFG $\eta = 0$ (i.e., the EFG is axially symmetric). This is reasonable based on

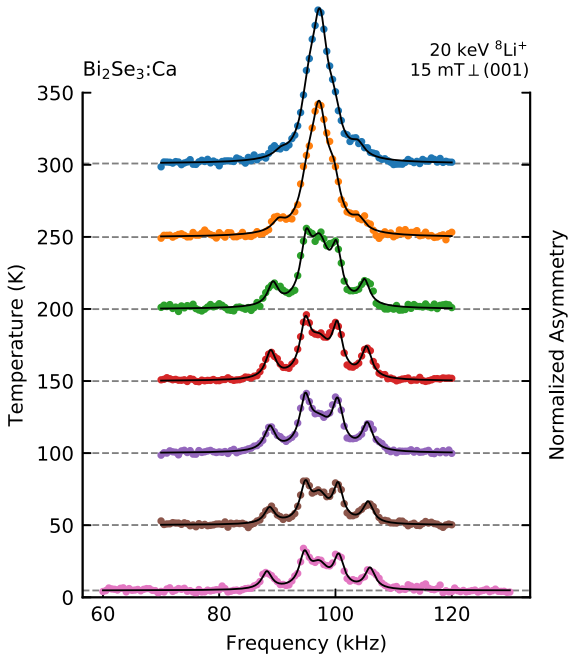

FIG. 3. ^{8}Li resonance spectra in BSC at low magnetic field. The vertical scale is the same for all spectra; they have been normalized to account for changes in intensity due to SLR [41], with their baselines (shown as dashed gray lines) shifted to match the temperature. The spectra consist of a small and nearly temperature-independent quadrupole split pattern, centered about an unsplit Lorentzian line, whose amplitude grows above ∼150 K. Note that the quadrupole pattern of an integer spin nucleus like ^{8}Li has no central satellite (main line). The solid black lines are fits to a sum of this Lorentzian plus and $2I = 4$ quadrupole satellites (see the text).

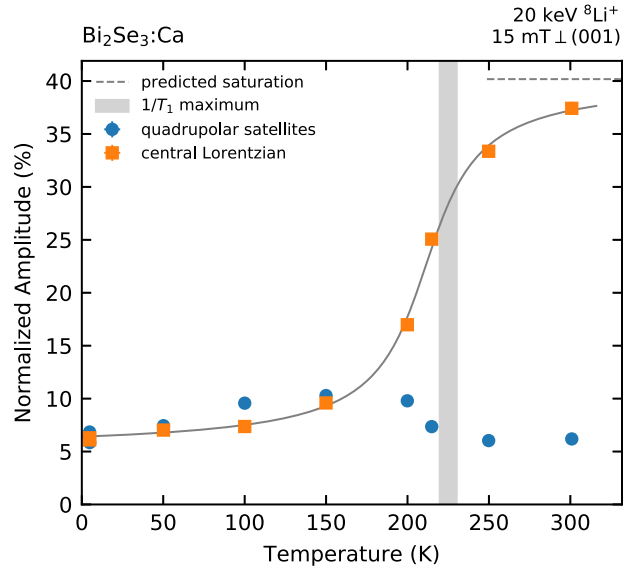

FIG. 4. The resonance amplitude as a function of temperature in Ca-doped Bi_2Se_3 at 15 mT. While the amplitude of the satellite lines is nearly temperature-independent, the central component increases substantially above 150 K, plateauing on the high-T side of the $1/T_1$ maximum (gray band). The solid line is a guide, while the dashed line indicates the estimated saturation value for the Lorentzian component.

likely interstitial sites for $^8Li^+$ [5]. Pairs of helicity-resolved spectra were fit with ν_0 and ν_q as shared free parameters, in addition to linewidths and amplitudes. As the difference between the frequency of the unsplit line and the center of the quadrupole split pattern was too small to measure accurately, the fits were additionally constrained to have the same central frequency ν_0. This is identical to the approach used for BTS [5]. A subset of the results (after recombining the two helicities) are shown in Fig. 3 as solid black lines.

The main result is the strong temperature dependence of the resonance amplitude shown in Fig. 4. While the satellite amplitudes are nearly temperature-independent, the central component increases substantially above 150 K, tending to plateau above the $1/T_1$ peak. The other parameters are quite insensitive to temperature. Typical linewidths (i.e., full width at half-maximum) are ∼2.2 kHz for the satellites and ∼3.8 kHz for the central component. The quadrupole frequency $\nu_q \approx 5.5$ kHz varies weakly, increasing slightly as temperature is lowered.

We also measured resonances at room and base temperature in high field (6.55 T) where ^{8}Li is sensitive to small magnetic shifts. From the fits, we use ν_0 to calculate the raw relative frequency shift δ in parts per million (ppm) using

$$\delta = 10^6\left(\frac{\nu_0 - \nu_{\mathrm{MgO}}}{\nu_{\mathrm{MgO}}}\right), \tag{6}$$

where ν_{MgO} is the reference frequency position in MgO at 300 K. The shifts are small: +12(2) ppm at room temperature and −17(3) ppm at 5 K, the latter considerably smaller in magnitude than in BTS [5]. Because ^{8}Li NMR shifts are generally so small, it is essential to account for the demagnetization field of the sample itself. From δ, the corrected shift K is obtained by the centimeter-gram-second system of units (CGS) expression [44]:

$$K = \delta + 4\pi\left(N - \frac{1}{3}\right)\chi_v, \tag{7}$$

where N is the dimensionless demagnetization factor that depends only on the shape of the sample, and χ_v is the dimensionless (volume) susceptibility. For a thin film, N is 1 [44], but for the thin platelet crystals used here, we estimate N is on the order of ∼0.8, treating them as oblate ellipsoids [45]. For the susceptibility, we take the average of literature values reported for pure Bi_2Se_3 [46–49], giving $\chi_v^{\mathrm{CGS}} \approx -2.4 \times 10^{-6}$ emu cm^{-3}. Note that we have excluded several reports [50–52] whose results disagree by an order of magnitude from those predicted by Pascal's constants [53]. Applying the correction for BSC yields K's of −2 (2) and −31 (3) ppm at room and base temperature, respectively. We discuss this below in Sec. IV B.

B. Bi_2Te_3:Mn

Typical ^{8}Li SLR spectra at high and low field in the magnetically doped BTM are shown in Fig. 5. In contrast to nonmagnetic BSC, the relaxation at high field is fast, typical of paramagnets with unpaired electron spins [54–56]. The fast high-field rate produces a much less pronounced field

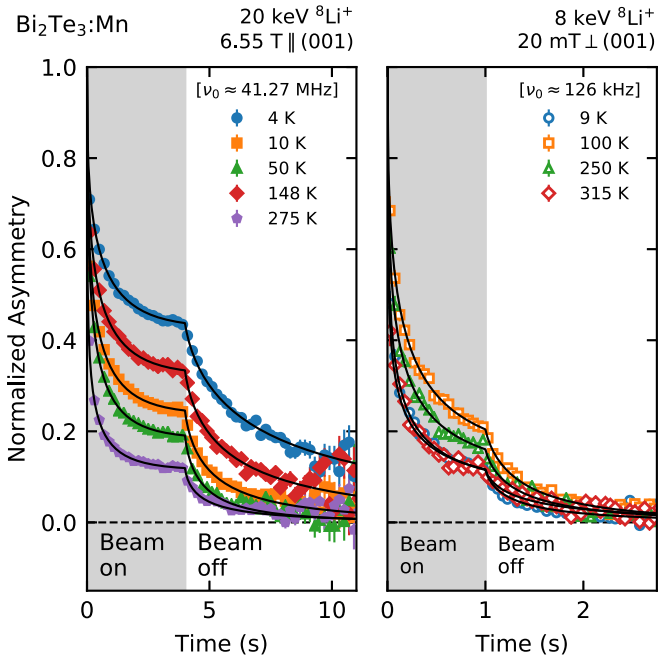

FIG. 5. Typical ^{8}Li SLR spectra in Mn-doped Bi_2Te_3 at high (left) and low (right) magnetic field for $^8Li^+$ implantation energies of 20 and 8 keV, respectively. The shaded region denotes the duration of the $^8Li^+$ beam pulse. The SLR is substantial and orders of magnitude faster than in BSC (see Fig. 1) at high field. The field dependence to the SLR is much weaker than in the nonmagnetic tetradymites. The solid black lines are fits to a stretched exponential convoluted with the $^8Li^+$ beam pulse as described in the text. The initial asymmetry A_0 from the fit is used to normalize the spectra. The high- and low-field spectra have been binned for by factors of 20 and 5, respectively.

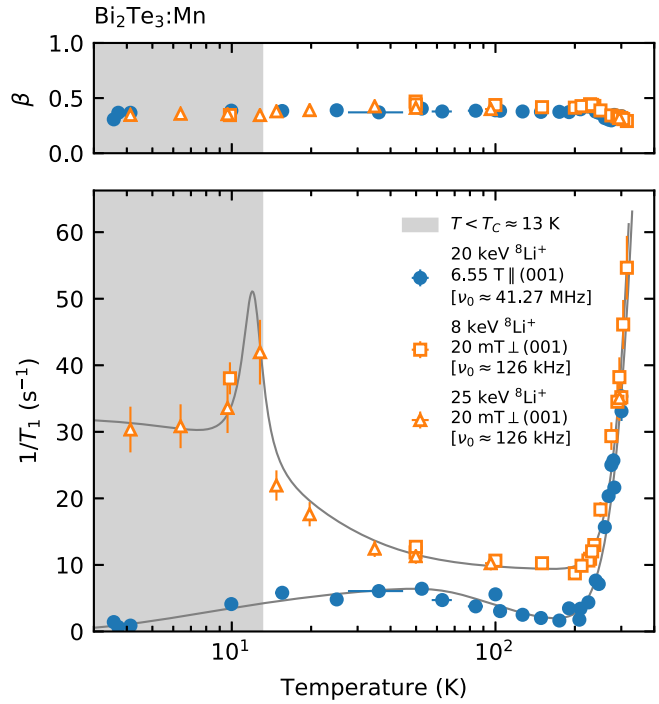

FIG. 6. Temperature dependence of the ^{8}Li SLR rate $1/T_1$ in Mn-doped Bi_2Te_3 at high and low field. At low field, $1/T_1$ shows a critical peak at the ferromagnetic transition at $T_C \approx 13$ K, as the Mn spin fluctuations freeze-out. Above 200 K, the SLR rate increases exponentially in a manner nearly independent of applied field. The solid gray lines are drawn to guide the eye.

dependence. At low field, the SLR rate is peaked at low temperature. The relaxation is also nonexponential and fits well using Eq. (1), with a stretching exponent systematically smaller than in the nonmagnetic BSC or BTS [5]. We analyzed the data with the same global approach, obtaining good quality fits ($\tilde{\chi}^2_{\text{global}} \approx 1.01$) demonstrated by the solid black lines in Fig. 5. The shared values of A_0 from the fits are large ($\sim$10% for $B_0 = 6.55$ T and $\sim$15% for $B_0 = 20$ mT), consistent with the full beam polarization, implying that there is remarkably no magnetic wipeout from very fast relaxation [54], even at low field.

The fit parameters are shown in Fig. 6. At all temperatures, especially at high field, the SLR rate $1/T_1$ is orders of magnitude larger than in the nonmagnetic analogs. No clear $1/T_1$ BPP peaks can be identified between 100 and 300 K; however, in the low-field data, a critical divergence is evident at the magnetometric transition at about 13 K. In high field, this feature is largely washed out, with a remnant peak near 50 K. Above 200 K, the SLR rate increases very rapidly and is well-described by $1/T_1 \propto \exp[-E_A/(k_B T)]$, with $E_A \approx 0.2$ eV at both fields. We discuss this below in Sec. IV A.

In contrast to BSC and BTS [5], the resonance in BTM consists of a single broad Lorentzian with none of the resolved fine structure (see Fig. 7). Surprisingly, the very broad line has significant intensity, dwarfing the quadrupole pattern in BSC in both width and amplitude. In addition, there is a large negative shift at 10 K. At room temperature, the line is somewhat narrower, and the shift is reduced in magnitude. Quantitative results from Lorentzian fits are summarized in Table II.

IV. DISCUSSION

The ^{8}Li NMR properties of nonmagnetic BSC are quite similar to previous measurements in BTS [5]. The resonance spectra show a similar splitting (ν_q is about 25% smaller in BSC), indicating a similar site for ^{8}Li. The resemblance of the spectra extends to the detailed temperature dependence, including the growth of the unsplit line approaching room temperature. Surprisingly, the BSC spectra are better resolved than BTS, implying a higher degree of order, despite the Ca doping. This is also evident in the SLR, with a stretching exponent β closer to unity in BSC than in BTS. This likely reflects additional disorder in BTS from Bi/Te antisite defects [57] that are much more prevalent than for Bi/Se, due to the difference in radii and electronegativity. The sharp quadrupolar pattern indicates a well-defined crystallographic $^8Li^+$ site, and the corresponding small EFG suggests it is in the vdW gap. Density functional theory (DFT) calculations of the EFG may enable a precise site assignment. The high-field SLR is also similar to BTS: it is slow and near the lower limit measurable due to the finite ^{8}Li lifetime τ_β and comparable to the vdW metal $NbSe_2$ [58], where the carrier concentration is much higher, but significantly slower than the TI alloy $Bi_{1-x}Sb_x$ [20]. The low-field enhancement of $1/T_1$ is also

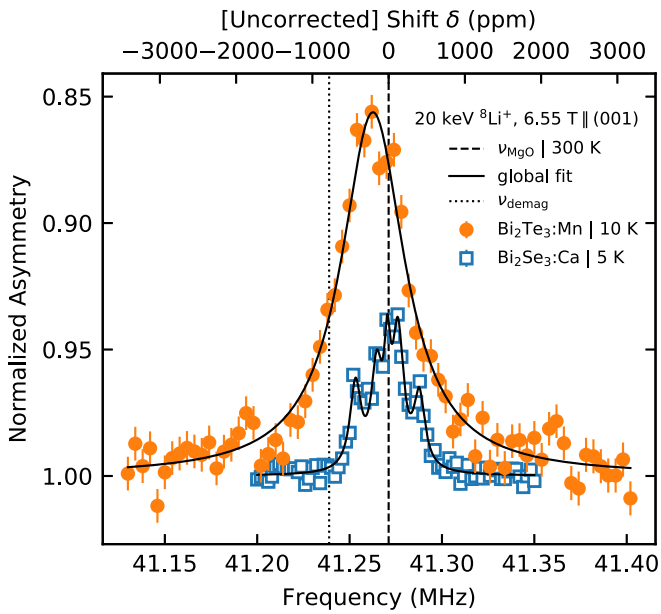

FIG. 7. Typical ^{8}Li resonances in Mn-doped Bi_2Te_3 and Ca-doped Bi_2Se_3 at high magnetic field. The vertical scale is the same for both spectra; they have been normalized to account for changes in intensity and baseline [41]. The line shape in the magnetic Bi_2Te_3 : Mn (BTM) is well-described by a broad Lorentzian (solid black line) with no quadrupolar splitting. A large negative shift is also apparent for BTM with respect to the reference frequency in MgO (vertical dashed line). The dotted vertical line indicates the expected resonance position due to demagnetization, revealing a large positive hyperfine field (∼38 G) at 5 K in the magnetic state.

similar, so it cannot be essentially related to the dilute ^{125}Te moments that are absent in BSC, but probably determined primarily by the 100% abundant ^{209}Bi. From such a detailed similarity, it is clear that a quantitative comparison with BTS and other vdW materials will be useful.

With these similarities in mind, the rest of the discussion is organized as follows: in Sec. IV A, we consider evidence of mobility of the ^{8}Li$^+$ ion; in Sec. IV B, we discuss the electronic effects at low temperature in BSC; and the magnetic properties of BTM are discussed in Sec. IV C.

A. Dynamics of the Li$^+$ ion

In BTS, we considered if the evolution of the spectrum with temperature (similar to Fig. 3) was the result of a site change transition from a metastable quadrupolar ^{8}Li$^+$ site to a lower energy site with very small EFG at higher temperature [5],

TABLE II. Results from the analysis of the ^{8}Li resonance in BTM at high and low temperature with $B_0 = 6.55$ T ∥ (001). The (bulk) magnetization M measured with 1.0 T ∥ (001) is included for comparison.

T (K)	$\tilde{A}$(%)	FWHM (kHz)	δ (ppm)	M (emu cm^{-3})
294	33 ± 5	16.2 ±1.2	+10 ± 9	0.076
10	14.4 ± 0.8	41.7± 1.6	−206 ± 12	7.698

similar to elemental Nb [59]. We now consider an alternative explanation, namely dynamic averaging of the quadrupolar interaction due to ^{8}Li$^+$ motion. Examples of this are found in conventional ^{7}Li NMR, where, unlike ^{8}Li, the $I = 3/2$ quadrupole spectrum has a main line (the $m = \pm 1/2$ satellite) overlapping the averaged resonance [60,61]. Dynamic averaging is suggested by the onset near, but below, the SLR rate peak (see Fig. 4). However, for hopping between equivalent interstitial sites (probably the quasioctahedral Wyckoff 3b site in the vdW gap—see Fig. 12 in Ref. [5]), one does not expect that the EFG will average to a value near zero (required to explain the unsplit line). A point charge estimate reveals that the quasitetrahedral (Wyckoff 6c) site, thought to be the saddle point in the potential for Li$^+$ between adjacent 3b sites [62], has an EFG of opposite sign to the 3b site. If 6c is instead a shallow minimum, the ^{8}Li$^+$ residence time there may be long enough that the EFG averages to near zero. In the fast motion limit at higher temperatures, one would then expect the quadrupole splitting to reemerge when the residence time in the 6c "transition" site becomes much shorter [61].

We now examine the two kinetic processes causing the $1/T_1$ peaks in BSC. It is surprising to find two distinct thermally activated processes sweeping through the NMR frequency, especially since only a single process was found in BTS [5]. First, we consider the weaker feature, i.e., the low temperature ($i = 1$) peaks. In layered materials, small intercalates can undergo highly localized motion at relatively low temperatures below the onset of free diffusion [22,23]. Such local motion may be the source of the SLR rate peak, but it is quite ineffective at narrowing the resonance, consistent with the absence of any line-shape changes in the vicinity of the $i = 1$ peaks. Caged local motion is usually characterized by a small activation barrier, comparable to the ∼0.1 eV observed here. Similar phenomena have been observed at low temperature, for example in neutron activated ^{8}Li β-NMR of Li intercalated graphite, LiC_{12} [63,64]. It is not clear why such motion would be absent in BTS [5], which has a larger vdW gap than BSC (2.698 versus 2.568 Å). Alternatively, this feature in the relaxation may have an electronic origin, perhaps related to the emergent low-T magnetism in $MoTe_2$ observed by μSR [65] and ^{8}Li β-NMR [66].

In contrast, the SLR rate peak above 200 K ($i = 2$) is almost certainly due to EFG fluctuations caused by stochastic ^{8}Li$^+$ motion. From the data, we cannot conclude that this is long-range diffusion, but the room-temperature Li$^+$ intercalability of Bi_2Se_3 [6–8] suggests it is. Its barrier, on the order of ∼0.4 eV, is comparable to other vdW gap layered ion conductors, but it is about twice as high as in BTS [5], possibly a result of the Se (rather than Te) bounded vdW gap, which provides less space between neighboring QLs.

We now consider the Arrhenius law prefactors τ_0^{-1}, that, for ionic diffusion, are typically in the range 10^{12}–10^{14} s^{-1}. For the low-T process ($i = 1$), independent of the form of J_n (see Table I), $\tau_0^{-1} \approx 9 \times 10^{10}$ s^{-1} is unusually low. In contrast, for the high-T ($i = 2$) process, it is much larger and depends strongly on J_n. For 3D diffusion, it is in the expected range, while the 2D model yields an extremely large value, $\sim 10^{16}$ s^{-1}, in the realm of prefactor anomalies [67] and opposite to the small value expected for low dimensional diffusion [68]. Similar behavior was observed recently in ^{7}Li

NMR of LiC_6 [69], where surprisingly, J_n^{2D} was concluded to be less appropriate than J_n^{3D}, suggesting that Li motion in the vdW gap is not as ideally 2D as might be expected. In BSC, the anomaly may be related to local dynamics that onset at lower T, imparting some 3D character to the motion.

Given the evidence for long-range Li^+ motion in BSC and BTS [5], the absence of a relaxation peak in BTM may seem unexpected. Both Ca^{2+} and Mn^{2+} dopants (substitutional for Bi^{3+}) have an effective -1 charge yielding an attractive trapping potential for the positive interstitial $^8Li^+$, but the Mn concentration is an order of magnitude larger. The high trap density in BTM will suppress Li^+ mobility. The exponential increase in $1/T_1$ above 200 K may be the onset of a diffusive BPP peak, but, in this case, one does not expect it to be so similar between the two very different magnetic fields. This may reflect a trade-off between the increase in ω_0 that shifts the peak to higher temperature, slowing the relaxation on its low-T flank, and the increased polarization of the Mn moments by the field that amplifies local magnetic inhomogeneities. A motional origin for this increase is consistent with the apparent $E_A \sim 0.2$ eV, similar to $^8Li^+$ in BTS [5], which also has a Te bounded vdW gap of similar size to BTM (2.620 Å). However, it may have a different explanation; see below in Sec. IV C.

B. Electronic effects at low temperature

Bismuth chalcogenide (Bi_2Ch_3) crystals exhibit substantial bulk conductivity, despite a narrow gap in the 3D band structure, making it difficult to distinguish effects of the metallic TSS. This is due to native defects (e.g., Ch vacancies) that are difficult or impossible to avoid [3]. Extrinsic dopants, such as substitutional Ca/Bi, can be used to compensate the spontaneous n-type doping. Brahlek *et al.* have argued [70] that, even for the most insulating compensated samples, the carrier densities far exceed the Mott criterion, making them heavily doped semiconductors in the metallic regime. In this case, we expect metallic NMR characteristics [71], namely a magnetic Knight shift K, proportional to the carrier spin susceptibility χ_s [72]. In the simplest (isotropic) case,

$$K = A\chi_s, \tag{8}$$

where A is the hyperfine coupling constant, which is accompanied by a SLR rate following the Korringa law [32,38],

$$\frac{1}{T_1} = 4\pi\hbar A^2\gamma_n^2\left(\frac{\chi_s}{g^*\mu_B}\right)^2 k_B T. \tag{9}$$

Here, γ_n is the nuclear gyromagnetic ratio, g^* is the carrier g-factor, and μ_B is the Bohr magneton. Combining Eqs. (8) and (9), we obtain the Korringa product, which is independent of the value of A,

$$T_1TK^2 = \frac{\hbar(g^*\mu_B)^2}{4\pi k_B\gamma_n} = S(g^*). \tag{10}$$

For ^8Li,

$$S(g^*) \approx 1.20 \times 10^{-5}\left(\frac{g^*}{g_0}\right)^2 \text{s K},$$

TABLE III. Korringa analysis of BSC and BTS [5] at 6.55 T and low temperature. To calculate $\mathscr{K}$, we take $S(g^*)$ in Eq. (11) to be 2.69×10^{-3} s K, using the $g_\parallel^*$ from EPR [74].

	$1/(T_1T)$ (10^{-6} s^{-1} K^{-1})	K (ppm)	$\mathscr{K}$
Bi_2Se_3:Ca	9.5 ± 0.8	-31 ± 3	0.038 ± 0.008
Bi_2Te_2Se	1.79 ± 0.07	-115 ± 3	2.78 ± 0.18

where, unlike in metals, we have allowed for an effective g-factor that may be far from its free electron value $g_0 \approx 2$ [73]. Indeed, recent electron paramagnetic resonance (EPR) measurements in Bi_2Se_3 find $g^* \approx 30$ [74].

According to Ref. [70], BTS and BSC lie on opposite sides of the Ioffe-Regel limit, where the carrier mean free path is equal to its Fermi wavelength, with BSC having a higher carrier density and mobility. A comparative Korringa analysis could test this assertion, and, to this end, using Eq. (10) we define the dimensionless Korringa ratio as

$$\mathscr{K} = \frac{T_1TK^2}{S(g^*)}. \tag{11}$$

Below the Ioffe-Regel limit, the autocorrelation function of the local hyperfine field at the nucleus, due to the carriers (that determines T_1), becomes limited by the diffusive transport correlation time. This has been shown to enhance the Korringa rate (i.e., shortening T_1) [75,76]. From this, one expects that $\mathscr{K}$ would be smaller in BTS than in BSC.

There are, however, significant difficulties in determining the experimental $\mathscr{K}$. First, the Korringa slope depends on magnetic field. At low fields, this is due to coupling with the host nuclear spins, a phenomenon that is quenched in high fields where the ^8Li NMR has no spectral overlap with the NMR of host nuclei. For example, in simple metals, we find the expected field-independent Korringa slope at high fields in the Tesla range [18]. In contrast, in BTS, the slope decreases substantially with increasing field, even at high fields [5]. We suggested this could be the result of magnetic carrier freeze-out. While we do not have comparably extensive data in BSC, we can compare the slope at the same field, 6.55 T (see Table III). Here, in both materials, the relaxation is extremely slow, exhibiting no curvature in the SLR during the ^8Li lifetime (Fig. 1), so the uncertainties in $1/T_1T$ are likely underestimates. The larger slope is, however, consistent with a higher carrier density n in BSC. The Korringa slopes should scale [73] as $n^{2/3}$. Using $n \sim 1 \times 10^{19}$ cm^{-3} in BSC [11] and $\sim 2 \times 10^{17}$ cm^{-3} in BTS [77], the slopes should differ by a factor of $\sim$14, while experimentally the ratio is $\sim$5.

The next difficulty is accurately quantifying the shift K, which is quite small with a relatively large demagnetization correction. Experimentally, the zero of shift, defined by the calibration in MgO, differs from the true zero (where $\chi_s = 0$) by the difference in chemical (orbital) shifts between MgO and the chalcogenide. However, because Li chemical shifts are universally very small, this should not be a large difference, perhaps a few ppm. The negative low temperature shift is also somewhat surprising. The hyperfine coupling A for Li is usually determined by a slight hybridization of the vacant $2s$ orbital with the host conduction band. As the s orbital

has density at the nucleus, the resulting coupling is usually positive, with the d-band metals Pd and Pt being exceptional [18]. For a positive A, the sign of K is determined by the sign of g^*, which has not yet been conclusively measured in either BSC or BTS. A more serious concern is that K depends on temperature (in contrast to simple metals) and, at least in BTS, also on applied field [5]. To avoid ambiguity from the field dependence, we similarly restrict comparison to the same field, 6.55 T. A similarly temperature-dependent shift (for the ^{207}Pb NMR) was found in the narrow band semiconductor PbTe [78], where it was explained by the temperature dependence of the Fermi level E_F [79]. At low-T in the heavily p-type PbTe, E_F occurs in the valence (or a nearby impurity) band, but with increasing temperature, it moves upward into the gap, causing a reduction in $|K|$. With this in mind, we assume the low temperature shift is the most relevant for a Korringa comparison. Without a measured g^* in BTS, we simply assume it is the same as BSC, and we use the $g^*_{\parallel}$ from EPR [74] to calculate the values of $\mathscr{K}$ in Table III.

The values of $\mathscr{K}$ are just opposite to the expectation of faster relaxation for diffusive BTS compared to metallic BSC [70]. Electronic correlations can, however, significantly alter the Korringa ratio to an extent that depends on disorder [80]. There should be no significant correlations in the broad bulk bands of the chalcogenides, but in narrow impurity bands this is certainly a possibility. We note that $\mathscr{K}$ is also less than 1 in PbTe [81], similar to BSC. At this stage, without more data and a better understanding of the considerations mentioned above, it is premature to draw further conclusions.

C. Magnetism in Bi_2Te_3 : Mn

In the Mn-doped Bi_2Te_3 at low field, the relaxation from magnetic Mn^{2+} becomes faster as the spin fluctuations slow down on cooling toward T_C. In particular, the low-T increase in $1/T_1$ occurs near where correlations among the Mn spins become evident in EPR [25,82]. In remarkable contrast to ferromagnetic EuO [54], the signal is not wiped out in the vicinity of T_C, but $1/T_1$ does become very fast. This is likely a consequence of a relatively small hyperfine coupling consistent with a Li site in the vdW gap.

High applied field slows the Mn spins more continuously starting from a higher temperature, suppressing the critical peak and reducing $1/T_1$ significantly, a well-known phenomenon in NMR and μSR at magnetic transitions (see, e.g., Ref. [83]). This also explains the small critical peak in the ^{8}Li SLR in the dilute magnetic semiconductor, $Ga_{1-x}Mn_xAs$ [56]. As in GaAs, Mn in Bi_2Te_3 is both a magnetic and electronic dopant. At this concentration, BTM is p-type with a metallic carrier density of $\sim 7 \times 10^{19}$ cm^{-3} [13,25]. However, the difference in scale of $1/T_1$ at high field between Figs. 2 and 6 shows that the Mn spins completely dominate the carrier relaxation.

It is also remarkable that the resonance is so clear in the magnetic state, in contrast to $Ga_{1-x}Mn_xAs$ [56]. The difference is not the linewidth, but rather the enhanced amplitude. This may be due to slow ^{8}Li spectral dynamics occurring on the timescale of τ_β that effectively enhance the amplitude, e.g., slow fluctuations of the ordered Mn moments, not far below T_C. Similar behavior was found in rutile TiO_2 at low temperature, where it was attributed to field fluctuations due to a nearby electron polaron [31]. Enhancement of the RF field at nuclei in a ferromagnet [84] may also play a role.

Above 200 K, the activated increase in $1/T_1$ may indicate the onset of diffusive $^8Li^+$ motion, similar to the nonmagnetic analogs, with the additional effect that the local magnetic field from the Mn spins is also modulated by ^{8}Li hopping (not just the EFG), similar to the ordered magnetic vdW layered $CrSe_2$ [85]. However, it may instead mark the onset of thermal excitation of electrons across the band gap that is narrowed by Mn doping [13]. Thermally excited carriers may also explain the increase in $1/T_1$ at comparable temperatures in $Ga_{1-x}Mn_xAs$ [56], a very different medium for Li^+ diffusion. Thermally increased carrier density would strengthen interaction between the Mn moments, extend their effects via Ruderman-Kittel-Kasuya-Yosida (RKKY) polarization, and increase $1/T_1$. Measurements at higher temperatures may be able to discriminate these possibilities, but it is likely that both processes will contribute.

The stretched SLR and field-dependent $1/T_1$ are characteristic of the NMR response in a disordered glassy magnetic state, consistent with the random Mn/Bi site disorder. The magnetic properties of BTM [13,24–26] are similar to the dilute (ferro)magnetic semiconductors that include a uniform magnetization of the carriers. In this context, our data provide a *local* characterization of the inhomogeneous magnetic state of BTM that will be useful in developing a detailed microscopic understanding of its magnetism. Having established the effects of Mn magnetism in the bulk, it would be interesting to use lower implantation energies to study how they may be altered in the surface region by coupling to the TSS.

V. CONCLUSION

Using implanted ^{8}Li β-NMR, we have studied the electronic and magnetic properties of the doped TIs BSC and BTM. From SLR measurements, we find evidence at temperatures above $\sim$200 K for site-to-site hopping of isolated Li^+ with an Arrhenius activation energy of $\sim$0.4 eV in BSC. At lower temperature the electronic properties dominate, giving rise to Korringa-like relaxation and negative Knight shifts, similar to isostructural BTS. A quantitative comparison reveals Korringa ratios opposite from expectations across the Ioffe-Regel limit. In BTM, the magnetism from dilute Mn moments dominates all other spin interactions, but the β-NMR signal remains measurable through the magnetic transition at T_C, where a critical peak in the SLR rate is observed. The $\sim$0.2 eV activation energy from the high-temperature increase in the SLR may be related to Li mobility or to thermal carrier excitations.

With these results, a more complete picture of the implanted ^{8}Li NMR probe of the tetradymite Bi chalcogenides (and other vdW chalcogenides) is beginning to emerge. At high temperatures, isolated $^8Li^+$ has a tendency to mobilize, providing unique access to the kinetic parameters governing Li^+ diffusion in the ultradilute limit. At low temperature, ^{8}Li is sensitive to the local metallic and magnetic properties of the host. With the bulk NMR response now established in Bi_2Ch_3 TIs, the prospect of directly probing the chiral TSS with the depth resolution provided by β-NMR remains promising.

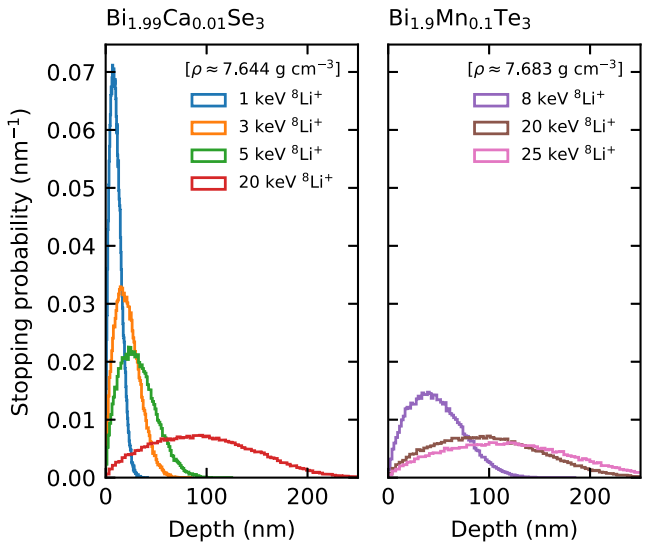

FIG. 8. Stopping distribution for ^{8}Li$^+$ implanted in the doped TIs BSC and BTM, calculated using the SRIM Monte Carlo code [27] using 10^5 ions. The implanted probe ions stop principally within ∼250 nm from the crystal surface, with only a minor "tail" penetrating further. Only at the lowest ^{8}Li$^+$ implantation energy 1 keV does an appreciable fraction (∼15%) stop in the region where surface effects are expected to be important.

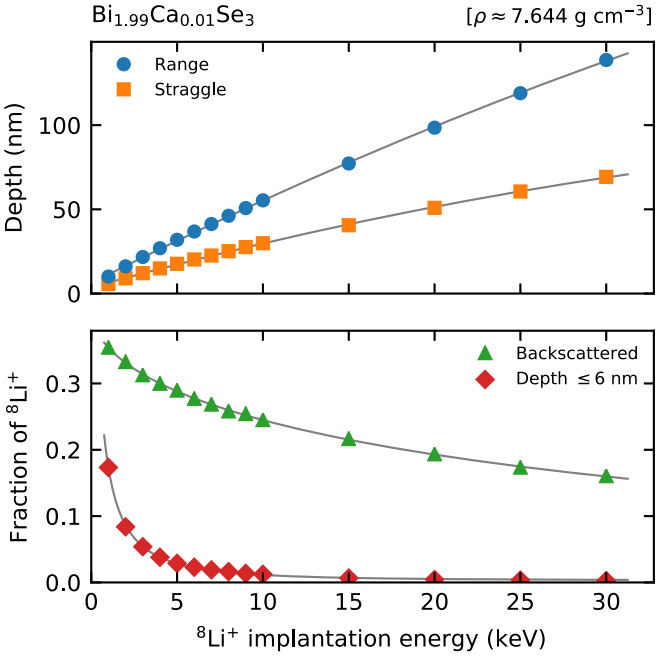

FIG. 9. Stopping details for ^{8}Li$^+$ implanted in BSC calculated using the SRIM Monte Carlo code [27]. The ion stopping range and straggle (i.e., mean and standard deviation) at each implantation energy are shown in the top panel. The bottom panel shows the predicted fraction of ^{8}Li$^+$ that are backscattered and those that stop within the first ∼6 nm, where surface effects are expected. Other than at the lowest implantation energy, this latter fraction is negligible. The solid gray lines are drawn to guide the eye.

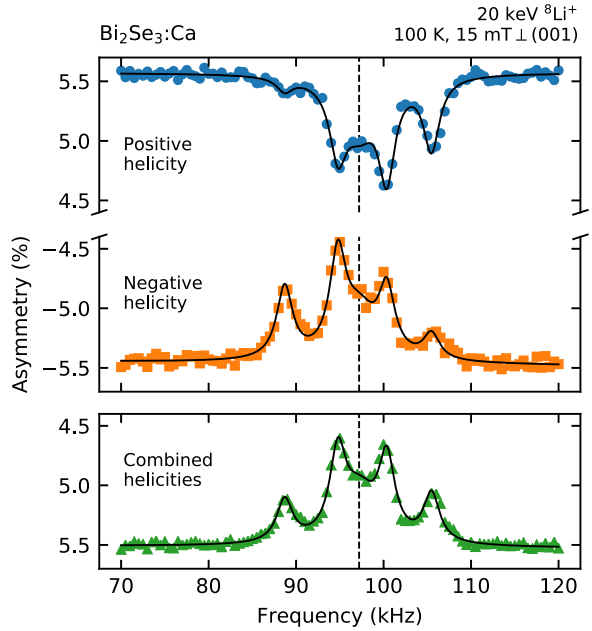

FIG. 10. Typical helicity-resolved ^{8}Li spectra in BSC, revealing the fine structure of the line. Four quadrupole satellites, split asymmetrically in each helicity about a "central" Lorentzian (marked by a vertical dashed line), are evident. Note that, in contrast to conventional NMR, the satellite amplitudes are determined primarily by the highly polarized initial state. The solid black lines are the fits described in the text, and the vertical dashed line marks the resonance central frequency ν_0.

ACKNOWLEDGMENTS

We thank R. Abasalti, D. J. Arseneau, S. Daviel, B. Hitti, K. Olchanski, and D. Vyas for their excellent technical support; M. H. Dehn, T. J. Parolin, O. Ofer, Z. Salman, Q. Song, and D. Wang for assistance with early measurements; as well as D. E. MacLaughlin, S. D. Senturia, and A. Wolos for useful discussions. This work was supported by NSERC Discovery grants to R.F.K. and W.A.M. Additionally, R.M.L.M. and A.C. acknowledge support from their NSERC CREATE IsoSiM Fellowships. The crystal growth at Princeton University was supported by the ARO-sponsored MURI on topological insulators, Grant No. W911NF1210461.

APPENDIX A: ^{8}Li$^+$ IMPLANTATION PROFILES

The SRIM Monte Carlo code [27] was used to predict the ^{8}Li$^+$ implantation profiles in BSC and BTM. At a given implantation energy, stopping events were simulated for 10^5 ions, which were histogrammed to represent the predicted implantation profile shown in Fig. 8. From the stopping profiles, we calculated, in the nomenclature of ion-implantation literature, the range and straggle (i.e., the mean and standard deviation) of the ^{8}Li$^+$ stopping depth. Additionally, the fraction of the simulated ions that were backscattered (i.e., did not stop in the target material), or stopped at very shallow depths below the surface, were determined for BSC (see Fig. 9). At the ion beam energies used here (1–25 keV), at most a small minority of the implanted ^{8}Li$^+$ ions stop in the top few nm where surface effects are anticipated. Thus, we do not expect a

significant contribution from the TSS. To study it will require an implantation energy substantially less than 1 keV.

APPENDIX B: HELICITY-RESOLVED RESONANCES

As mentioned in Sec. II, unique to ion-implanted β-NMR, the probe nuclear spin polarization is produced *ex situ* using collinear optical pumping [28]. The projection of the nuclear spin on the beam direction (the helicity) is either "positive" or "negative" depending on the sense (left or right) of the circularly polarized laser light, which is alternated during each measurement. Data are collected separately for each laser helicity yielding helicity-resolved spectra, which are useful at elucidating details of the resonance [18].

A typical helicity-resolved ^{8}Li resonance spectrum in BSC is shown in Fig. 10. Besides the well-resolved fine structure, the spectra unambiguously reveal the multicomponent nature of the line. A quadrupolar splitting, giving the antisymmetric shape about the resonance center-of-mass in each helicity, on the order of several kHz, can be identified from the outermost satellites. In contrast to conventional NMR, note that the satellite intensities are chiefly determined by the high initial polarization, causing an increase in the relative amplitude of the outer satellites [29], which also depend on the SLR. Apart from the quadrupolar component, another contribution at the resonance "center," with no resolved splitting, is discernible. This is consistent with the ^{8}Li resonances observed in other vdW materials [5,58,85]. Unlike the more common case encountered for the spin $I = 3/2$ ^{7}Li nucleus, there is no $m_{\pm 1/2} \leftrightarrow m_{\mp 1/2}$ main line transition that is unshifted in first-order by the quadrupolar interaction. The absence of any peaks interlacing the $m_{\pm 2} \leftrightarrow m_{\pm 1}$ transitions suggests this "central" line cannot be multiquantum (cf. the spectrum in Bi [20,29]). Instead, the "central" peak must originate from ^{8}Li in an environment where the static (i.e., time-average) EFG is close to zero. For presentation, we combined the helicity-resolved spectra to give an overall average line shape (Fig. 3 in Sec. III A).

[1] D. Hsieh, Y. Xia, D. Qian, L. Wray, J. H. Dil, F. Meier, J. Osterwalder, L. Patthey, J. G. Checkelsky, N. P. Ong, A. V. Fedorov, H. Lin, A. Bansil, D. Grauer, Y. S. Hor, R. J. Cava, and M. Z. Hasan, A tunable topological insulator in the spin helical dirac transport regime, Nature (London) **460**, 1101 (2009).

[2] H. Zhang, C.-X. Liu, X.-L. Qi, X. Dai, Z. Fang, and S.-C. Zhang, Topological insulators in Bi_2Se_3, Bi_2Te_3 and Sb_2Te_3 with a single dirac cone on the surface, Nat. Phys. **5**, 438 (2009).

[3] R. J. Cava, H. Ji, M. K. Fuccillo, Q. D. Gibson, and Y. S. Hor, Crystal structure and chemistry of topological insulators, J. Mater. Chem. C **1**, 3176 (2013).

[4] J. P. Heremans, R. J. Cava, and N. Samarth, Tetradymites as thermoelectrics and topological insulators, Nat. Rev. Mater. **2**, 17049 (2017).

[5] R. M. L. McFadden, A. Chatzichristos, K. H. Chow, D. L. Cortie, M. H. Dehn, D. Fujimoto, M. D. Hossain, H. Ji, V. L. Karner, R. F. Kiefl, C. D. Philip Levy, R. Li, I. McKenzie, G. D. Morris, O. Ofer, M. R. Pearson, M. Stachura, R. J. Cava, and W. A. MacFarlane, Ionic and electronic properties of the topological insulator Bi_2Te_2Se investigated via β-detected nuclear magnetic relaxation and resonance of ^{8}Li, Phys. Rev. B **99**, 125201 (2019).

[6] K. Paraskevopoulos, E. Hatzikraniotis, K. Chrisafis, M. Zamani, J. Stoemenos, N. A. Economou, K. Alexiadis, and M. Balkanski, Intercalation studies in bismuth selenide, Mater. Sci. Eng., B **1**, 147 (1988).

[7] C. Julien, I. Sararas, and A. Chevy, Studies of lithium insertion in bismuth chalcogenide compounds, Solid State Ionics **36**, 113 (1989).

[8] J. Bludská, I. Jakubec, S. Karamazov, J. Horák, and C. Uher, Lithium ions in the van der Waals gap of Bi_2Se_3 single crystals, J. Solid State Chem. **183**, 2813 (2010).

[9] M. S. Whittingham, Chemistry of intercalation compounds: Metal guests in chalcogenide hosts, Prog. Solid State Chem. **12**, 41 (1978).

[10] R. H. Friend and A. D. Yoffe, Electronic properties of intercalation complexes of the transition metal dichalcogenides, Adv. Phys. **36**, 1 (1987).

[11] Y. S. Hor, A. Richardella, P. Roushan, Y. Xia, J. G. Checkelsky, A. Yazdani, M. Z. Hasan, N. P. Ong, and R. J. Cava, *p*-type Bi_2Se_3 for topological insulator and low-temperature thermoelectric applications, Phys. Rev. B **79**, 195208 (2009).

[12] Y. L. Chen, J.-H. Chu, J. G. Analytis, Z. K. Liu, K. Igarashi, H.-H. Kuo, X. L. Qi, S. K. Mo, R. G. Moore, D. H. Lu, M. Hashimoto, T. Sasagawa, S. C. Zhang, I. R. Fisher, Z. Hussain, and Z. X. Shen, Massive Dirac fermion on the surface of a magnetically doped topological insulator, Science **329**, 659 (2010).

[13] Y. S. Hor, P. Roushan, H. Beidenkopf, J. Seo, D. Qu, J. G. Checkelsky, L. A. Wray, D. Hsieh, Y. Xia, S.-Y. Xu, D. Qian, M. Z. Hasan, N. P. Ong, A. Yazdani, and R. J. Cava, Development of ferromagnetism in the doped topological insulator $Bi_{2-x}Mn_xTe_3$, Phys. Rev. B **81**, 195203 (2010).

[14] Y. Tokura, K. Yasuda, and A. Tsukazaki, Magnetic topological insulators, Nat. Rev. Phys. **1**, 126 (2019).

[15] D. M. Nisson, A. P. Dioguardi, P. Klavins, C. H. Lin, K. Shirer, A. C. Shockley, J. Crocker, and N. J. Curro, Nuclear magnetic resonance as a probe of electronic states of Bi_2Se_3, Phys. Rev. B **87**, 195202 (2013).

[16] D. Koumoulis, B. Leung, T. C. Chasapis, R. Taylor, D. King, M. G. Kanatzidis, and L.-S. Bouchard, Understanding bulk defects in topological insulators from nuclear-spin interactions, Adv. Funct. Mater. **24**, 1519 (2014).

[17] E. M. Levin, T. M. Riedemann, A. Howard, N. H. Jo, S. L. Bud'ko, P. C. Canfield, and T. A. Lograsso, ^{125}Te NMR and Seebeck effect in Bi_2Te_3 synthesized from stoichiometric and Te-rich melts, J. Phys. Chem. C **120**, 25196 (2016).

[18] W. A. MacFarlane, Implanted-ion βNMR: A new probe for nanoscience, Solid State Nucl. Magn. Reson. **68–69**, 1 (2015).

[19] G. D. Morris, β-NMR, Hyperfine Interact. **225**, 173 (2014).

[20] W. A. MacFarlane, C. B. L. Tschense, T. Buck, K. H. Chow, D. L. Cortie, A. N. Hariwal, R. F. Kiefl, D. Koumoulis, C. D. P. Levy, I. McKenzie, F. H. McGee, G. D. Morris, M. R. Pearson, Q. Song, D. Wang, Y. S. Hor, and R. J. Cava, β-detected NMR of $^8Li^+$ in Bi, Sb, and the topological insulator $Bi_{0.9}Sb_{0.1}$, Phys. Rev. B **90**, 214422 (2014).

[21] N. Bloembergen, E. M. Purcell, and R. V. Pound, Relaxation effects in nuclear magnetic resonance absorption, Phys. Rev. **73**, 679 (1948).

[22] O. Kanert, Dynamical properties of defects in solids, Phys. Rep. **91**, 183 (1982).

[23] W. Müller-Warmuth, Structure, bonding, dynamics: NMR studies, in *Progress in Intercalation Research*, Physics and Chemistry of Materials with Low-Dimensional Structures, edited by W. Müller-Warmuth and R. Schöllhorn (Springer, Dordrecht, 1994), Vol. 17, pp. 339–455.

[24] M. D. Watson, L. J. Collins-McIntyre, L. R. Shelford, A. I. Coldea, D. Prabhakaran, S. C. Speller, T. Mousavi, C. R. M. Grovenor, Z. Salman, S. R. Giblin, G. van der Laan, and T. Hesjedal, Study of the structural, electric and magnetic properties of Mn-doped Bi_2Te_3 single crystals, New J. Phys. **15**, 103016 (2013).

[25] S. Zimmermann, F. Steckel, C. Hess, H. W. Ji, Y. S. Hor, R. J. Cava, B. Büchner, and V. Kataev, Spin dynamics and magnetic interactions of Mn dopants in the topological insulator Bi_2Te_3, Phys. Rev. B **94**, 125205 (2016).

[26] D. Vaknin, D. M. Pajerowski, D. L. Schlagel, K. W. Dennis, and R. J. McQueeney, Two-dimensional ordering and collective magnetic excitations in the dilute ferromagnetic topological insulator $(Bi_{0.95}Mn_{0.05})_2Te_3$, Phys. Rev. B **99**, 220404(R) (2019).

[27] J. F. Ziegler, J. P. Biersack, and M. D. Ziegler, *SRIM—The Stopping and Range of Ions in Matter*, 7th ed. (SRIM, Chester, MD, 2008).

[28] C. D. P. Levy, M. R. Pearson, R. F. Kiefl, E. Mané, G. D. Morris, and A. Voss, Laser polarization facility, Hyperfine Interact. **225**, 165 (2014).

[29] W. A. MacFarlane, C. D. P. Levy, M. R. Pearson, T. Buck, K. H. Chow, A. N. Hariwal, R. F. Kiefl, F. H. McGee, G. D. Morris, and D. Wang, The initial state of optically polarized $^8Li^+$ from the β-NMR in bismuth, J. Phys.: Conf. Ser. **551**, 012059 (2014).

[30] H. Ackermann, P. Heitjans, and H.-J. Stöckmann, β emitters and isomeric nuclei as probes in condensed matter, in *Hyperfine Interactions of Radioactive Nuclei*, Topics in Current Physics Vol. 31, edited by J. Christiansen (Springer, Berlin, 1983), Chap. 6, pp. 291–361.

[31] R. M. L. McFadden, T. J. Buck, A. Chatzichristos, C.-C. Chen, K. H. Chow, D. L. Cortie, M. H. Dehn, V. L. Karner, D. Koumoulis, C. D. P. Levy, C. Li, I. McKenzie, R. Merkle, G. D. Morris, M. R. Pearson, Z. Salman, D. Samuelis, M. Stachura, J. Xiao, J. Maier, R. F. Kiefl, and W. A. MacFarlane, Microscopic dynamics of Li^+ in rutile TiO_2 revealed by ^8Li β-detected nuclear magnetic resonance, Chem. Mater. **29**, 10187 (2017).

[32] C. P. Slichter, *Principles of Magnetic Resonance*, 3rd ed., Springer Series in Solid-State Sciences Vol. 1 (Springer, Berlin, 1990).

[33] M. D. Hossain, Z. Salman, D. Wang, K. H. Chow, S. Kreitzman, T. A. Keeler, C. D. P. Levy, W. A. MacFarlane, R. I. Miller, G. D. Morris, T. J. Parolin, M. Pearson, H. Saadaoui, and R. F. Kiefl, Low-field cross spin relaxation of ^8Li in superconducting $NbSe_2$, Phys. Rev. B **79**, 144518 (2009).

[34] F. James and M. Roos, MINUIT—A system for function minimization and analysis of the parameter errors and correlations, Comput. Phys. Commun. **10**, 343 (1975).

[35] R. Brun and F. Rademakers, ROOT—An object oriented data analysis framework, Nucl. Instrum. Methods Phys. Res., Sect. A **389**, 81 (1997).

[36] P. M. Richards, Magnetic resonance in superionic conductors, in *Physics of Superionic Conductors*, Topics in Current Physics, edited by M. B. Salamon, Vol. 15 (Springer, Berlin, 1979), Chap. 6, pp. 141–174.

[37] P. A. Beckmann, Spectral densities and nuclear spin relaxation in solids, Phys. Rep. **171**, 85 (1988).

[38] J. Korringa, Nuclear magnetic relaxation and resonance line shift in metals, Physica **16**, 601 (1950).

[39] W. Küchler, P. Heitjans, A. Payer, and R. Schöllhorn, ^7Li NMR relaxation by diffusion in hexagonal and cubic Li_xTiS_2, Solid State Ionics **70–71**, 434 (1994).

[40] Note that the large A_0 down to low field precludes $^8Li^+$ sites with very large EFGs.

[41] M. D. Hossain, H. Saadaoui, T. J. Parolin, Q. Song, D. Wang, M. Smadella, K. H. Chow, M. Egilmez, I. Fan, R. F. Kiefl, S. R. Kreitzman, C. D. P. Levy, G. D. Morris, M. R. Pearson, Z. Salman, and W. A. MacFarlane, The spin lattice relaxation of ^8Li in simple metals, Physica B **404**, 914 (2009).

[42] M. H. Cohen and F. Reif, Quadrupole effects in nuclear magnetic resonance studies of solids, in *Solid State Physics*, edited by F. Seitz and D. Turnbull (Academic, San Diego, 1957), Vol. 5, pp. 321–438.

[43] F. Taulelle, NMR of quadrupolar nuclei in the solid state, in *Multinuclear Magnetic Resonance in Liquids and Solids—Chemical Applications*, NATO ASI Series C: Mathematical and Physical Sciences, edited by P. Granger and R. K. Harris (Springer, Dordrecht, 1990), Vol. 322, Chap. 21, pp. 393–407.

[44] M. Xu, M. D. Hossain, H. Saadaoui, T. J. Parolin, K. H. Chow, T. A. Keeler, R. F. Kiefl, G. D. Morris, Z. Salman, Q. Song, D. Wang, and W. A. MacFarlane, Proximal magnetometry in thin films using βNMR, J. Magn. Res. **191**, 47 (2008).

[45] J. A. Osborn, Demagnetizing factors of the general ellipsoid, Phys. Rev. **67**, 351 (1945).

[46] M. Matyáš, The susceptibility of selenides and tellurides of heavy elements, Czech. J. Phys. **8**, 309 (1958).

[47] V. A. Kulbachinskii, A. Y. Kaminsky, K. Kindo, Y. Narumi, K. ichi Suga, P. Lostak, and P. Svanda, Low temperature ferromagnetism in the new diluted magnetic semiconductor p-$Bi_{2-x}Fe_xTe_3$, Physica B **329–333**, 1251 (2003).

[48] A. S. Panfilov, G. E. Grechnev, A. V. Fedorchenko, K. Conder, and E. V. Pomjakushina, Magnetic properties of Mn-doped Bi_2Se_3 compound: temperature dependence and pressure effects, J. Phys.: Condens. Matter **27**, 456002 (2015).

[49] S. V. Chong, G. V. M. Williams, and R. L. Moody, The effect of manganese incorporation in Bi_2Se_3 on the thermal, electrical transport and magnetic properties, J. Alloys Compd. **686**, 245 (2016).

[50] P. Janíček, Č. Drašar, P. Lošt'ák, J. Vejpravová, and V. Sechovský, Transport, magnetic, optical and thermodynamic properties of $Bi_{2-x}Mn_xSe_3$ single crystals, Physica B **403**, 3553 (2008).

[51] B.-L. Young, Z.-Y. Lai, Z. Xu, A. Yang, G. D. Gu, Z.-H. Pan, T. Valla, G. J. Shu, R. Sankar, and F. C. Chou, Probing the bulk electronic states of Bi_2Se_3 using nuclear magnetic resonance, Phys. Rev. B **86**, 075137 (2012).

[52] L. Zhao, H. Deng, I. Korzhovska, Z. Chen, M. Konczykowski, A. Hruban, V. Oganesyan, and L. Krusin-Elbaum, Singular robust room-temperature spin response from topological Dirac fermions, Nat. Mater. **13**, 580 (2014).

[53] G. A. Bain and J. F. Berry, Diamagnetic corrections and Pascal's constants, J. Chem. Ed. **85**, 532 (2008).

[54] W. A. MacFarlane, Q. Song, N. J. C. Ingle, K. H. Chow, M. Egilmez, I. Fan, M. D. Hossain, R. F. Kiefl, C. D. P. Levy, G. D. Morris, T. J. Parolin, M. R. Pearson, H. Saadaoui, Z. Salman, and D. Wang, β-detected NMR spin relaxation in a thin film heterostructure of ferromagnetic EuO, Phys. Rev. B **92**, 064409 (2015).

[55] D. L. Cortie, T. Buck, M. H. Dehn, V. L. Karner, R. F. Kiefl, C. D. P. Levy, R. M. L. McFadden, G. D. Morris, I. McKenzie, M. R. Pearson, X. L. Wang, and W. A. MacFarlane, β-NMR Investigation of the Depth-Dependent Magnetic Properties of an Antiferromagnetic Surface, Phys. Rev. Lett. **116**, 106103 (2016).

[56] Q. Song, K. H. Chow, Z. Salman, H. Saadaoui, M. D. Hossain, R. F. Kiefl, G. D. Morris, C. D. P. Levy, M. R. Pearson, T. J. Parolin, I. Fan, T. A. Keeler, M. Smadella, D. Wang, K. M. Yu, X. Liu, J. K. Furdyna, and W. A. MacFarlane, β-detected NMR of Li in $Ga_{1-x}Mn_xAs$, Phys. Rev. B **84**, 054414 (2011).

[57] D. O. Scanlon, P. D. C. King, R. P. Singh, A. de la Torre, S. M. Walker, G. Balakrishnan, F. Baumberger, and C. R. A. Catlow, Controlling bulk conductivity in topological insulators: Key role of anti-site defects, Adv. Mater. **24**, 2154 (2012).

[58] D. Wang, M. D. Hossain, Z. Salman, D. Arseneau, K. H. Chow, S. Daviel, T. A. Keeler, R. F. Kiefl, S. R. Kreitzman, C. D. P. Levy, G. D. Morris, R. I. Miller, W. A. MacFarlane, T. J. Parolin, and H. Saadaoui, β-detected NMR of ^{8}Li in the normal state of $2H$-$NbSe_2$, Physica B **374–375**, 239 (2006).

[59] T. J. Parolin, J. Shi, Z. Salman, K. H. Chow, P. Dosanjh, H. Saadaoui, Q. Song, M. D. Hossain, R. F. Kiefl, C. D. P. Levy, M. R. Pearson, and W. A. MacFarlane, Nuclear magnetic resonance study of Li implanted in a thin film of niobium, Phys. Rev. B **80**, 174109 (2009).

[60] C. Galven, J. Dittmer, E. Suard, F. Le Berre, and M.-P. Crosnier-Lopez, Instability of lithium garnets against moisture. structural characterization and dynamics of $Li_{7-x}H_xLa_3Sn_2O_{12}$ and $Li_{5-x}H_xLa_3Nb_2O_{12}$, Chem. Mater. **24**, 3335 (2012).

[61] S. Indris, P. Heitjans, R. Uecker, and B. Roling, Li ion dynamics in a $LiAlO_2$ single crystal studied by ^{7}Li NMR spectroscopy and conductivity measurements, J. Phys. Chem. C **116**, 14243 (2012).

[62] M. A. Gosálvez, M. M. Otrokov, N. Ferrando, A. G. Ryabishchenkova, A. Ayuela, P. M. Echenique, and E. V. Chulkov, Low-coverage surface diffusion in complex periodic energy landscapes: Analytical solution for systems with symmetric hops and application to intercalation in topological insulators, Phys. Rev. B **93**, 075429 (2016).

[63] A. Schirmer, P. Heitjans, W. Faber, and J. E. Fischer, Spin-lattice relaxation of ^{8}Li in LiC_{12} at low temperatures, Synth. Met. **34**, 589 (1989).

[64] A. Schirmer and P. Heitjans, Diffusive motion in stage-1 and stage-2 Li-graphite intercalation compounds: Results of β-NMR and quasielastic neutron scattering, Z. Naturforsch. A **50**, 643 (1995).

[65] Z. Guguchia, A. Kerelsky, D. Edelberg, S. Banerjee, F. von Rohr, D. Scullion, M. Augustin, M. Scully, D. A. Rhodes, Z. Shermadini, H. Luetkens, A. Shengelaya, C. Baines, E. Morenzoni, A. Amato, J. C. Hone, R. Khasanov, S. J. L. Billinge, E. Santos, A. N. Pasupathy, and Y. J. Uemura, Magnetism in semiconducting molybdenum dichalcogenides, Sci. Adv. **4**, eaat3672 (2018).

[66] J. A. Krieger *et al.* (unpublished).

[67] M. Villa and J. L. Bjorkstam, Prefactor anomalies, Solid State Ionics **9**, 1421 (1983).

[68] P. M. Richards, Effect of low dimensionality on prefactor anomalies in superionic conductors, Solid State Commun. **25**, 1019 (1978).

[69] J. Langer, V. Epp, P. Heitjans, F. A. Mautner, and M. Wilkening, Lithium motion in the anode material LiC_6 as seen via time-domain ^{7}Li NMR, Phys. Rev. B **88**, 094304 (2013).

[70] M. Brahlek, N. Koirala, N. Bansal, and S. Oh, Transport properties of topological insulators: Band bending, bulk metal-to-insulator transition, and weak anti-localization, Solid State Commun. **215–216**, 54 (2015).

[71] D. F. Holcomb, Magnetic properties of doped semiconductors and tungsten bronzes, in *The Metal Non-Metal Transition in Disordered Systems*, edited by L. R. Friedman and D. P. Tunstall (Scottish Universities Summer School in Physics, Edinburgh, 1978), pp. 251–284.

[72] The NMR shift K is comprised of several terms including both the spin and orbital response of all the surrounding electrons. In metals, where the local carrier density is substantial, the Fermi contact coupling with the electron spins often dominates, as we have assumed here.

[73] D. C. Look and D. L. Moore, Nuclear-magnetic-resonance measurement of the conduction-electron g factor in CdTe, Phys. Rev. B **5**, 3406 (1972).

[74] A. Wolos, S. Szyszko, A. Drabinska, M. Kaminska, S. G. Strzelecka, A. Hruban, A. Materna, M. Piersa, J. Borysiuk, K. Sobczak, and M. Konczykowski, g-factors of conduction electrons and holes in Bi_2Se_3 three-dimensional topological insulator, Phys. Rev. B **93**, 155114 (2016).

[75] W. W. Warren, Nuclear magnetic resonance and relaxation in the "liquid semiconductors" In_2Te_3, Ga_2Te_3, and Sb_2Te_3, Phys. Rev. B **3**, 3708 (1971).

[76] W. Götze and W. Ketterle, Nuclear spin relaxation in disordered conductors, Z. Phys. B **54**, 49 (1983).

[77] S. Jia, H. Ji, E. Climent-Pascual, M. K. Fuccillo, M. E. Charles, J. Xiong, N. P. Ong, and R. J. Cava, Low-carrier-concentration crystals of the topological insulator Bi_2Te_2Se, Phys. Rev. B **84**, 235206 (2011).

[78] C. R. Hewes, M. S. Adler, and S. D. Senturia, Nuclear-magnetic-resonance studies in PbTe and $Pb_{1-x}Sn_xTe$: An experimental determination of $\vec{k}\cdot\vec{p}$ band parameters and magnetic hyperfine constants, Phys. Rev. B **7**, 5195 (1973).

[79] S. D. Senturia, A. C. Smith, C. R. Hewes, J. A. Hofmann, and P. L. Sagalyn, Knight shifts and band structure in the lead-salt semiconductors, Phys. Rev. B **1**, 4045 (1970).

[80] B. S. Shastry and E. Abrahams, What Does the Korringa Ratio Measure? Phys. Rev. Lett. **72**, 1933 (1994).

[81] M. N. Alexander, P. L. Sagalyn, S. D. Senturia, and C. R. Hewes, Nuclear spin relaxation study of the electronic structure of lead telluride, J. Nonmetals **1**, 251 (1973).

[82] Y. Talanov, V. Sakhin, E. Kukovitskii, N. Garif'yanov, and G. Teitel'baum, Magnetic resonance study of the Bi_2Te_3 doped with manganese, Appl. Magn. Reson. **48**, 143 (2017).

[83] R. H. Heffner, J. E. Sonier, D. E. MacLaughlin, G. J. Nieuwenhuys, G. M. Luke, Y. J. Uemura, W. Ratcliff, S.-W. Cheong, and G. Balakrishnan, Muon spin relaxation study of $La_{1-x}Ca_xMnO_3$, Phys. Rev. B **63**, 094408 (2001).

[84] A. C. Gossard and A. M. Portis, Observation of Nuclear Resonance in a Ferromagnet, Phys. Rev. Lett. **3**, 164 (1959).

[85] J. O. Ticknor, I. Umegaki, R. M. L. McFadden, A. Chatzichristos, D. Fujimoto, V. L. Karner, R. F. Kiefl, S. Kobayashi, C. D. P. Levy, R. Li, G. D. Morris, M. R. Pearson, K. Yoshimura, J. Sugiyama, and W. A. MacFarlane, Investigation of ionic and anomalous magnetic behavior in $CrSe_2$ using ^{8}Li β-NMR, RSC Adv. **10**, 8190 (2020).